Original Article

Computational simulation of the multiphasic degeneration of the bone-cartilage unit during osteoarthritis via indentation and unconfined compression tests

Seyed Shayan Sajjadinia[1], Mohammad Haghpanahi[*1], Mohammad Razi[2]

[1]School of Mechanical Engineering, Iran University of Science and Technology, Tehran 16846, Iran

[2]Department of Orthopedic Surgery and Department of sports medicine, Iran University of Medical Sciences, Tehran 14665-354, Iran

ABSTRACT

It has been experimentally proposed that the discrete regions of articular cartilage (AC), along with different subchondral bone (SB) tissues, known as the bone-cartilage unit (BCU), are biomechanically altered during osteoarthritis (OA) degeneration. However, a computational framework capturing all of the dominant changes in the multiphasic parameters has not yet been developed. This paper proposes a new BCU finite element (FE) model by combining several validated, nonlinear, depth-dependent, fibril-reinforced, and swelling models, which can computationally simulate the variations in the dominant parameters during OA degeneration by indentation and unconfined compression (UC) tests. The mentioned dominant parameters include the proteoglycan depletion, collagen

---
[*] Corresponding author (mhaghpanahi@iust.ac.ir)

fibrillar softening, permeability and fluid fraction increase for approximately non-advanced OA. The results depict the importance of SB tissues in fluid distribution within BCU by decreasing the fluid permeation and pressure (up to a maximum of 100 KPa) during OA, supporting the notion that SBs might play a role in the pathogenesis of OA. Furthermore, the OA composition-based studies shed light on the significant biomechanical role of the calcified cartilage (CC), which experienced a maximum change of 70 KPa in stress, together with relative load contributions of AC constituents during OA, in which the osmotic pressure bore around 70% of the loads after degeneration. To conclude, the new insights provided by the results reveal the significance of the multiphasic OA simulation and demonstrate the functionality of the proposed BCU model.

Keywords:

Introduction

Osteoarthritis (OA) is the most common form of the degenerative joint disease with sociological and financial impacts on health care systems [1,2]. Although previous studies have characterized this condition as the articular cartilage (AC) wear and tear, contemporary studies suggest that OA is a whole knee joint disorder leading to pain and loss of function without chronic autoimmune mechanisms [3–5]. In particular, it was experimentally and also computationally observed that different subchondral bone (SB) tissues have a contributory role in the biomechanical and biochemical degenerative behavior of AC [6–9]. However, a small proportion of OA researches elaborated such key role [5,10].

In the case of non-advanced OA, the bone-cartilage unit (BCU) permeability increases and the AC constituents damage depth-dependently [7,11,12]. The term bone-cartilage unit (BCU), as was firstly introduced by Lories and Luyten [5] and based on which some FE models were proposed [12,13], consists of several hydrated soft and hard tissues, namely the AC, calcified cartilage (CC), subchondral cortical bone (SCB), and subchondral trabecular bone (STB).

Moreover, the AC itself has a multiphasic fibril-reinforced and heterogeneous structure, in which the proteoglycans and predominant type II collagen fibers govern the nonlinear and anisotropic compression-tension response of the tissue [14], which should not be underestimated [15]. The interplay of AC constituents gives rise to the osmotic pressure coming from biochemical factors [16–18] and excellent biotribological properties [19]. Also, the interstitial fluid pressurization induces a dominant-transient drag force, especially in AC, which potentially supports most of the applied load [19,20]. Depending on the simulation procedures, incorporating all of the above-mentioned properties into a computational OA analysis is of high importance, yet it is challenging [21].

For the simulation of the multi-tissue pathogenesis of OA, which ideally involves whole knee joints, several FE simulations were carried out, although with a great deal of

simplifying the constitutive equations [22,23]. Nonetheless, they did not take into account the important osmotic pressure. Indeed, it is quite cumbersome to simulate the knee joint with its geometrical features and encompass an initially pre-stress state [24,25]. However, by drastically simplifying geometries, the foregoing could be introduced, such as the tissue plugs in tissue-scale studies [13,26].

In this study, a new BCU model was developed on the basis of the former well-established FE models. This computational model provides a more comprehensive description of BCU enabling it to perform a multiphasic simulation of OA degeneration by comparing the healthy and degenerated BCU through a set of UC and indentation FE tests. The functionality of the proposed model has been assessed, which also elucidates the role of the constituents in OA. To our knowledge, no previous study has aimed at simulating such OA degeneration which takes account of all the dominant multiphasic factors. To this aim, the importance of such multiphasic simulation was assessed by comparing the results with their counterparts in the previous studies.

Materials and methods

Constitutive model
Basically, the AC could be modeled by standard biphasic theory described by Mow et al. [27]. However, the AC Cauchy stress is contributed by the non-fibrillar $\boldsymbol{\sigma}^{MAT}$, fibrillar $\boldsymbol{\sigma}^{COL}$, and glycosaminoglycan (GAG) $\boldsymbol{\sigma}^{GAG}$ parts. By considering the fluid pressure p, the AC total stress $\boldsymbol{\sigma}^{TOT}$ becomes

$$\boldsymbol{\sigma}^{TOT} = \boldsymbol{\sigma}^{COL} + \boldsymbol{\sigma}^{MAT} - \boldsymbol{\sigma}^{GAG} - p\mathbf{I} \tag{1}$$

The Cauchy stress of the tensile fibrillar and modified Neo-Hookean non-fibrillar tensors was adapted from the previous research [28] as follows

$$\boldsymbol{\sigma}^{COL} = \frac{\phi_0^S}{J} \sum_{I=1}^{9} \left(\lambda^I \rho_C^I \left(E_0 + E_\varepsilon \varepsilon_F^I \right) \varepsilon_F^I \mathbf{n}^I \otimes \mathbf{n}^I \right) \qquad \varepsilon_F^I > 0 \tag{2}$$

$$\boldsymbol{\sigma}^{MAT} = \phi_0^S \left(1 - \rho_C^{TOT} \right) \left[-\frac{\ln J}{6J} G_m \left(\frac{J \phi_0^S 3 \ln J}{\left(\phi_0^S - J \right)^2} - 1 - 3 \frac{J + \phi_0^S}{J - \phi_0^S} \right) \mathbf{I} + \frac{G_m}{J} \left(\mathbf{F} \cdot \mathbf{F}^T - J^{2/3} \mathbf{I} \right) \right] \tag{3}$$

Where ϕ_0^S is the initial solid volume fraction parameter, $\mathbf{F}$ the deformation gradient tensor, J the volumetric deformation, G_m the shear modulus, E_0 and E_ε the initial and strain-dependent collagen coefficients (due to collagen stiffening). Also, $\mathbf{n}^I$, λ^I, ρ_C^I, ε_F^I are the current fibril direction, elongation, relative collagen fibril volume fraction, and logarithmic strain of the *Ith* fibril, respectively. This formulation ignores any AC viscosity as in our compression simulations, the only dominant transient respond might be corresponding to the fluid pressurization [29].
The collagen network was assumed to be a combination of two large primary fibrils according to the arcade-like orientation [30,31] and seven smaller secondary fibrils. Bundles of the dominant primary fibrils extend perpendicular from the subchondral surface, bend in opposite directions in AC middle zone to become parallel to the AC surface. The secondary fibrils are orientated in the direction of each axis and between them. The fibril densities were derived by [32]

$$\rho_C^I = \begin{cases} \dfrac{\rho_C^{TOT}}{2C^F+7}C^F & \text{(Primary fibrils)} \\[3mm] \dfrac{\rho_C^{TOT}}{2C^F+7} & \text{(Secondary fibrils)} \end{cases}$$

(4)

Where C^F is a positive constant, and ρ_C^{TOT} the depth-dependent total collagen volume fraction per total solid volume.

Furthermore, an extended two compartmental swelling stress model [33] was used to model the AC GAG constituent, as it potentially would provide a more accurate description of the degenerated AC than the ideal Donnan model [24,34]. The GAG Cauchy stress is given by

$$\boldsymbol{\sigma}^{GAG} = \hat{\alpha}_1\left(\frac{1}{J}\right)^{\alpha_2}\mathbf{I}$$

(5)

Where $\hat{\alpha}_1$ and α_2 are GAG material constants.

As the AC finite strains may lead to the void ratio e changes, a depth- and strain-dependent permeability function was chosen [35–38]

$$k = k_0\left(\frac{e}{e_0}\right)^{\kappa}\exp\left(\frac{M}{2}\left[\left(\frac{1+e}{1+e_0}\right)^2 - 1\right]\right)$$

(6)

Where k_0 is the zero-strain permeability, e_0 the initial void ratio, κ and M the material constants.

On the other hand, the subchondral regions were approximated by a biphasic mixture with an isotropic elastic solid phase and equivalent fluid phase [12]. Therefore, they are governed by their Young's modulus E_b and Poisson's ratio ν_b and permeability k_b parameters. A comprehensive list of material properties is shown in Table 1.

Table 1 - BCU material parameters: The BCU permeability and SB parameters were collected by Stender et al. [12] from previous works [7,39–46]. Taffetani et al. [47] measured GAG material coefficients depth-dependently via the procedure proposed by Stender et al. [24]. Also, the fibrillar and non-fibrillar material coefficients of the healthy AC was gathered by Wilson et al. [28] from former studies [32,48–50]. The changes in softened AC were adapted from previous works [51–53]. Generally, these properties were supposed to simulate a generalized BCU model rather than a specific type.

Material Parameter	Intact	Degenerated
$E_\varepsilon\,(MPa)$	3670	917.5
$E_0\,(MPa)$	4.63	
$G_m\,(MPa)$	0.723	
$C^F\,(-)$	3.009	
$\alpha_2\,(-)$	3.22	

$\hat{\alpha}_1\,(MPa)$	Layer 1: 0.005 Layer 2: 0.010 Layer 3: 0.025 Layer 4: 0.035 Layer 5: 0.042 Layer 6: 0.048 Layer 7: 0.053 Layer 8: 0.058 Layer 9: 0.060	
$\rho_c^{tot}\,(-)$	$1.4z^2 - 1.1z + 0.59$	
$\phi^S\,(-)$	$0.1 + 0.1z$	$0.05 + 0.1z$
$k_0\left(mm^2.s^{-1}/MPA\right)$	SZ: 6.81×10^{-3} MZ: 2.16×10^{-3} DZ: 0.74×10^{-3}	SZ: 4.55×10^{-3} MZ: 1.46×10^{-3} DZ: 0.5×10^{-3}
$M\,(-)$	SZ: 5.48, MZ: 5.49, DZ: 7.38	
$k_b\left(mm^2.s^{-1}/MPA\right)$	140	90
$E_b\,(MPa)$	CC: 320, SCB: 3900, STB: 1019	
$\nu_b\,(-)$	0.03	

Implementation

The BCU FE model was solved with the aid of the soil consolidation theory in Abaqus (v6.14, Simulia). However, the AC effective solid parts should be implemented via a user-defined material (UMAT) subroutine. Before running the analysis (step 0), the continuous depth-dependent material parameters had been calculated in each AC integration point from the normalized depth parameter (z) by the SDVINI subroutine. Subsequently, the calculated parameters were transferred to the UMAT subroutine by the state variables (STATEV). Then, a static (equilibrium) step was run to account for the pre-stress effects on the AC solid matrix due to GAG molecules reactions (Figure 1). As the UMAT subroutine makes use of Newton's method for the sake of FE linearization, the fourth-order consistent Jacobian tensor should be defined, which is a function of the right Cauchy-Green deformation tensor $\mathbf{C}$. This tensor is defined as
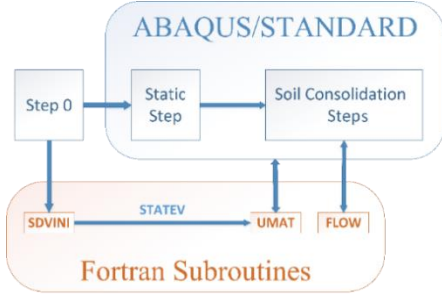
$$\mathbf{C} = \mathbf{F}^T \cdot \mathbf{F} \tag{7}$$

Figure 1. The interplay between Abaqus steps and different Fortran subroutines.

To derive the consistent Jacobian tensor $^4c_{ijkr}$, the following equation was suggested [54] in indicial notation

$$^4c_{ijkr} = \frac{1}{2}\left(\delta_{ri}\sigma_{kj}^{EFF} + \delta_{kj}\sigma_{ir}^{EFF} + \delta_{ki}\sigma_{rj}^{EFF} + \delta_{rj}\sigma_{ik}^{EFF}\right) + {}^4\tilde{c}_{ijkl} \tag{8}$$

Where δ is the Kronecker delta, and $^4\tilde{c}_{ijkr}$ the fourth-order spatial elasticity tensor which is

$$^4\tilde{c}_{ijkr} = \frac{1}{J}\left[F_{ip}F_{jq}F_{kl}F_{rs}\left({}^4\tilde{C}_{pqls}\right)\right] \tag{9}$$

Also, $^4\tilde{C}_{pqls}$ is the corresponding fourth-order material elasticity tensor, which should be computed for each of the AC solid parts by

$$^4\tilde{\mathbf{C}} = 2\frac{\partial \mathbf{S}}{\partial \mathbf{C}} \tag{10}$$

Where $\mathbf{S}$ is the 2nd Piola–Kirchhoff stress tensor, which is related to the Cauchy stress tensor by

$$\mathbf{S} = J\mathbf{F}^{-1}\cdot\boldsymbol{\sigma}\cdot\mathbf{F}^{-T} \tag{11}$$

Therefore, the fourth-order elasticity tensor should be derived for each part by the above-mentioned equations as follows

$$^4c_{ijkr} = \frac{1}{2}\left(\delta_{ri}\sigma_{kj}^{EFF} + \delta_{kj}\sigma_{ir}^{EFF} + \delta_{ki}\sigma_{rj}^{EFF} + \delta_{rj}\sigma_{ik}^{EFF}\right) + {}^4\tilde{c}_{ijkr}^{COL} + {}^4\tilde{c}_{ijkr}^{MAT} + {}^4\tilde{c}_{ijkr}^{GAGs} \tag{12}$$

Where $^4\tilde{c}_{ijkr}^{COL}$, $^4\tilde{c}_{ijkr}^{MAT}$, $^4\tilde{c}_{ijkr}^{GAGs}$ are respectively the fibrillar, non-fibrillar, and GAG spatial elasticity tensors. The latter was previously derived as [47]

$$^4\tilde{c}_{ijkr}^{GAG} = \hat{\alpha}_1\left(\frac{1}{J}\right)^{\alpha_2}\left[(\alpha_2 - 1)\delta_{ij}\delta_{kr} + \delta_{ik}\delta_{jr} + \delta_{ir}\delta_{jk}\right] \tag{13}$$

The other constituent elasticity tensors were derived in Appendix as

$$^4\tilde{c}_{ijkr}^{COL} = \frac{\phi_0^S}{J}\sum_{I=1}^{9}\left(\rho_C^I\lambda^I\left[E_0 + 2E_\varepsilon\varepsilon_F^I - \left(E_0 + E_\varepsilon\varepsilon_F^I\right)\varepsilon_F^I\right]n_i^I n_j^I n_k^I n_r^I\right) \tag{14}$$

$$^4\tilde{c}_{ijkr}^{MAT} = \phi_0^S\left(1 - \rho_C^{TOT}\right)\left(\begin{array}{l} \dfrac{G_m}{J}\left(J^{2/3} + \dfrac{\ln J}{6}\left[\dfrac{3n_{s,0}}{J - n_{s,0}}\left(\dfrac{J\ln J}{J - n_{s,0}} - 2\right) - 4\right]\right)\left(\delta_{ik}\delta_{jr} + \delta_{ir}\delta_{jk}\right) \\ -\dfrac{G_m}{2}\left(\dfrac{4J^{2/3} - 4 + \dfrac{3\phi_0^S}{J - \phi_0^S}\left(\dfrac{J\ln J}{J - \phi_0^S} - 2\right)}{3J} + \dfrac{(\ln J - 1)\phi_0^S\ln J}{\left(J - \phi_0^S\right)^2}\right)\delta_{ij}\delta_{kr} \end{array}\right) \tag{15}$$

6

Simulations

To investigate the OA multiphasic degeneration effects, the tests were simulated for the healthy and degenerated BCU models by an approach similar to the previous studies [12,51], where the thickness of AC SZ, MZ and deep zone (DZ), as well as CC, SCB, and STB regions were assumed to be 1.5mm, 5.0mm, 3.5mm, 0.05mm, 10mm, 10mm, respectively. Also, all the dominant parameters were altered during the non-advanced OA according to the recent study [11].

The UC test was simulated by 620 four-node axisymmetric quadrilateral, bilinear displacement and pore pressure elements with full integration (CAX4P). The nodal displacements at the bottom rigid impermeable platen were confined. The BCU, 10mm in diameter, was axially compressed by a rigid impermeable platen up to 1% strain. After relaxation, an additional 5% strain at a ramp-strain rate of $0.001Sec^{-1}$ took place, and then the platen was held unchanged to allow for full relaxation; meanwhile, the reaction force was recorded.

As to the indentation test, 1722 identical elements were utilized. The nodes at the bottom of BCUs were completely constrained. The BCU diameter was increased to 70mm to prevent any edge effects in AC. The indentation loading was applied by a 5% strain of the impermeable indenter (Figure 2) at a strain rate of $0.05Sec^{-1}$, with subsequent unloading back to the initial location during 2Sec, while the reaction force was recoded. The impermeable indenter, 25mm in diameter, was modeled with a small fillet of radius 0.3mm at the sharp corner in order to avoid the induced-stress concentration. The nodal displacements at the bottom impermeable plane of the BCUs were confined, while a biphasic contact condition was prescribed, in which the free fluid flow was allowed in the top BCU surface that is not in contact. This contact condition was prescribed by a FLOW subroutine, which requires identifying the seepage coefficient and reference sink pressure parameters. For our material constitutive equations, the foregoing parameters were assumed to be $1mm^3/N.s$ and 0, respectively [55].
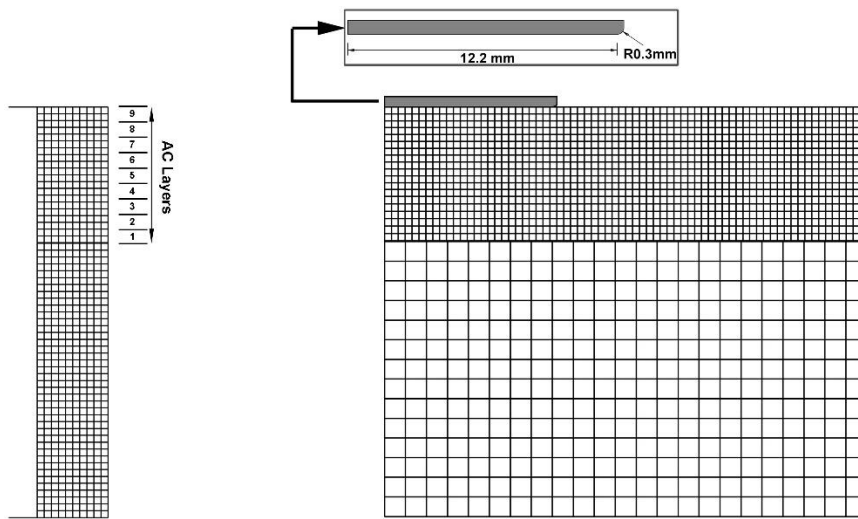

Figure 2. Axisymmetric FE models for UC simulation (left) and indentation simulation (right).

As explained in the preceding section, a static step were implemented for 1 Sec before implementing the main simulations (Figure 1). Following this step in the indentation tests and the first relaxation in the UC tests, the vertical Cauchy stresses in the BUC parts were calculated to evaluate the functionality of the proposed model. Also, the displacements of the nodes at the symmetry axis of all of the models were confined in the radial direction while zero pore pressure was imposed on the radial boundaries.

In addition to implementing a mesh refinement study and comparing the results of this study with the previous experimental data, two other experimental tests were simulated once again by the proposed model to evaluate the validity of the model. Accordingly, a UC test [56], plus a confined compression experiment [57], which was also replicated by another validated FE model [28], were implemented. Readers are referred to the corresponding papers for a more detailed description of the tests.

Results

OA simulation

Figure 3 represents the results of the pore pressure and fluid velocity vector for the healthy and degenerated BCU in the indentation test. While a 30% decrease in the fluid velocity is discernable in subchondral regions, the pore pressure decreased by a maximum of around 100 KPa in AC. This test shows a huge diminished peak reaction force during OA degeneration (Figure 4). Also, the mesh refinement study of the reaction force demonstrates sufficient mesh convergence by roughly a 50% reduction of the element numbers. Another point to consider is that the AC boundary near CC involves some distortions due to the AC pre-stress condition, which produced oscillating values. These inaccuracies are far from the region of interest and therefore did not interrupt the validity of the results.
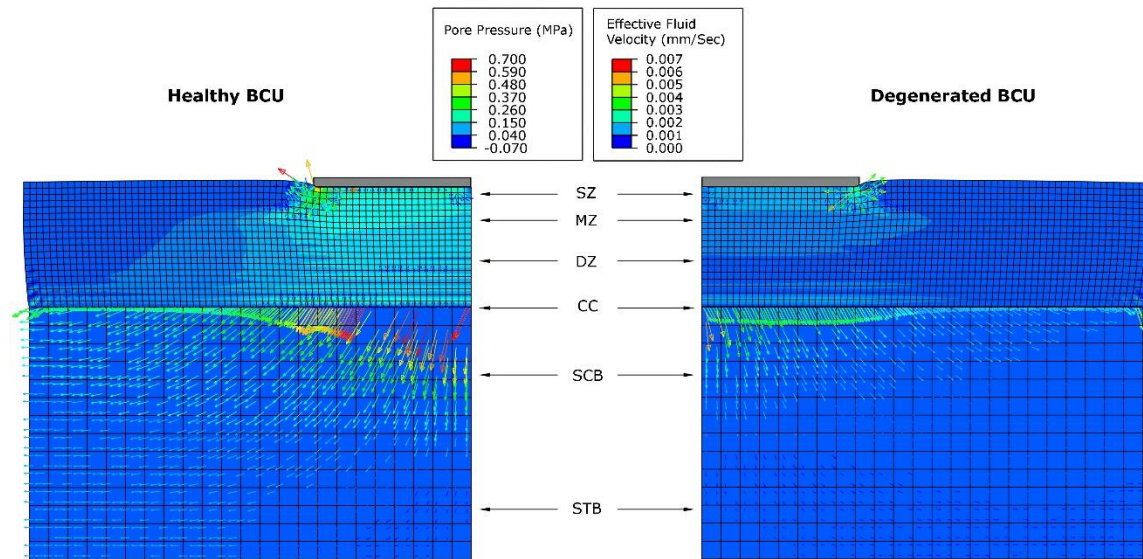

Figure 3. FE indentation simulation results for interstitial pore pressure and fluid velocity at peak load (just before the unloading step).
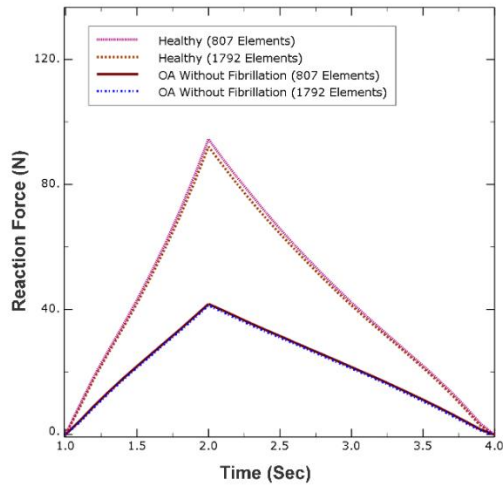
Figure 4. Plots of reaction force vs. time for the indentation test.

The contributions of the AC phases, near the subchondral zones, to vertical load sharings were depicted in percent (Figure 5). During OA, the load support was mainly shifted from the fluid pressure to the other AC phases, particularly the osmotic pressure, which also decreased depth-wisely (Figure 6).
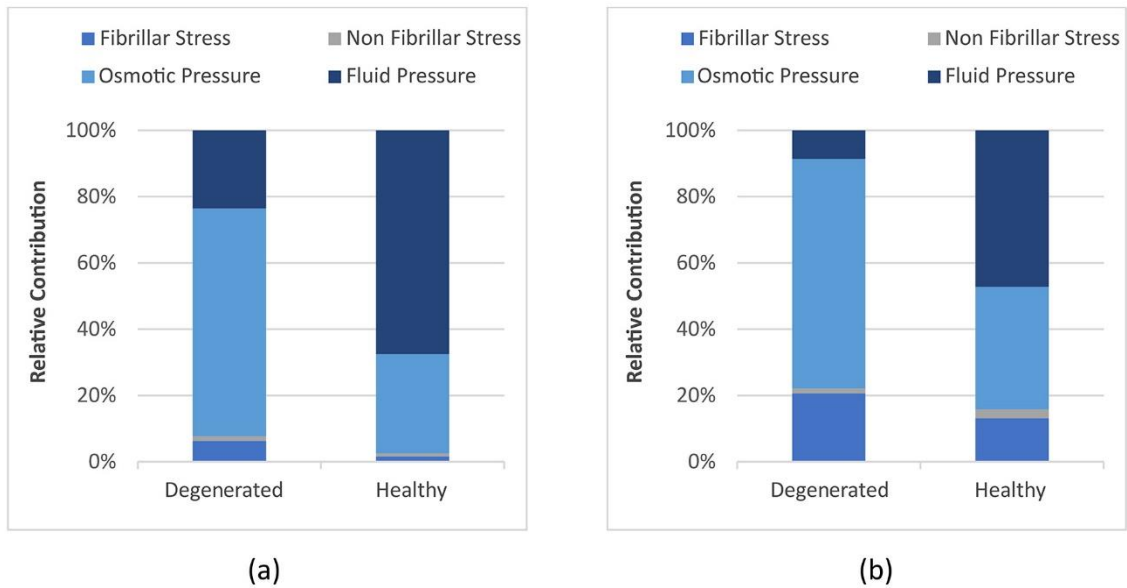

Figure 5. Contribution of AC components to normal load sharing in the DZ near the SBs at peak loads in (a) UC and (b) indentation tests.
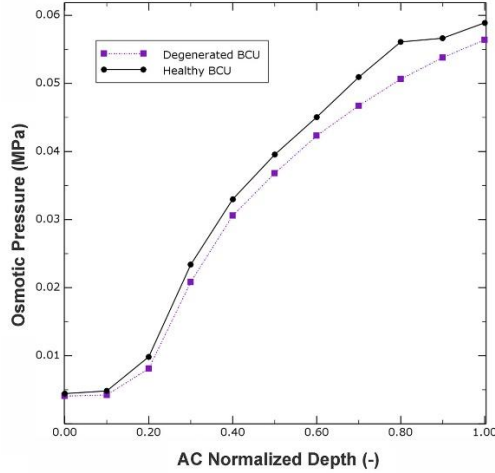
Figure 6. Plots of osmotic pressure vs. AC normalized depth (z) for indentation analysis at peak load.

       The recorded reaction forces in both compression tests declined by roughly 50% after OA while the stresses in the AC parts mainly decreased, with the exception of the fibrillar stresses, which increased after OA (10 KPa in peak loads), and the non-fibrillar stresses, which were more or less zero in all tests (Figure 7). Also, the recorded stresses in subchondral regions fell after OA, where the CC and STB respectively correspond to the lowest and highest stresses in UC tests, and these regions respectively contributed the most and the least to the load bearings in the indentation tests (Figure 8). The magnitudes of the osmotic pressure and non-fibrillar stress did not substantially vary during each different analysis; meanwhile, the fluid and fibrillar phases experienced upward and downward trends, respectively. After OA, the fluid part witnessed the most significant falls in stress (around 30 KPa in UC and 80 KPa in indentation tests), and the fibrillar part went up by around 10 KPa in both tests at peak loads. During unloading, the values of fluid pressure, unlike other BCU parts, did not follow the same paths as the loading steps to reach zero and experienced the maximum decreases of roughly 40 KPa and 10 KPa before and after OA, respectively. During stress relaxation, the stresses in the fluid and CC parts first peaked then reduced, whereas the stresses in the other AC phases did not vary dramatically, and the subchondral stresses went down. Among peak stresses in different subchondral regions, the CC saw the most drastic drops in stress during OA (70 and 53 KPa in indentation and UC tests, respectively).
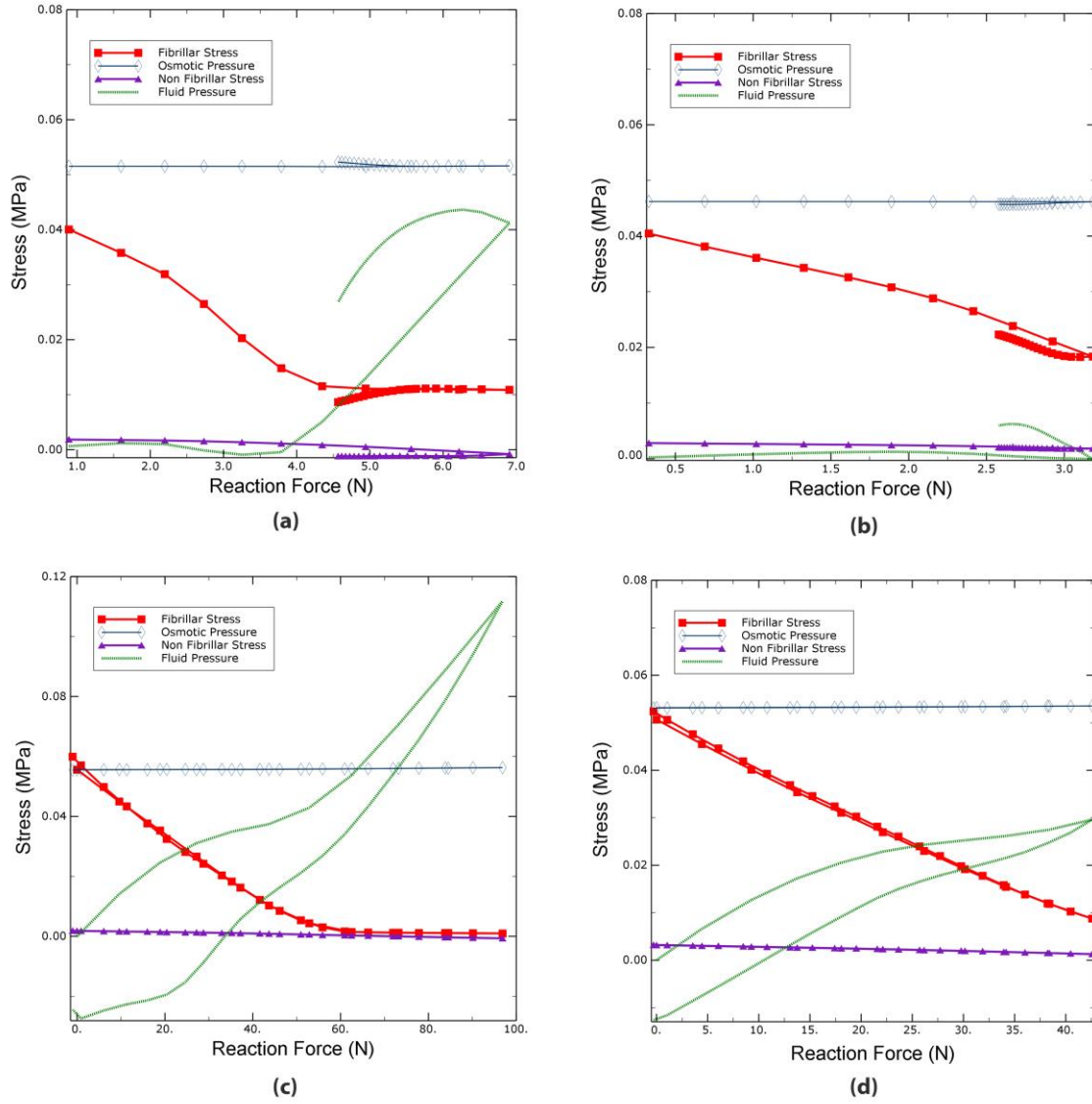
Figure 7. Stress in different phases of AC, near the SBs, as a function of recorded reaction force during UC tests on (a) healthy and (b) degenerated BCUs, plus indention tests on (c) healthy and (d) degenerated BCUs.

Figure 8. Stress in subchondral regions as a function of recorded reaction force during UC tests on (a) healthy and (b) degenerated BCUs, plus indention tests on (c) healthy and (d) degenerated BCUs.
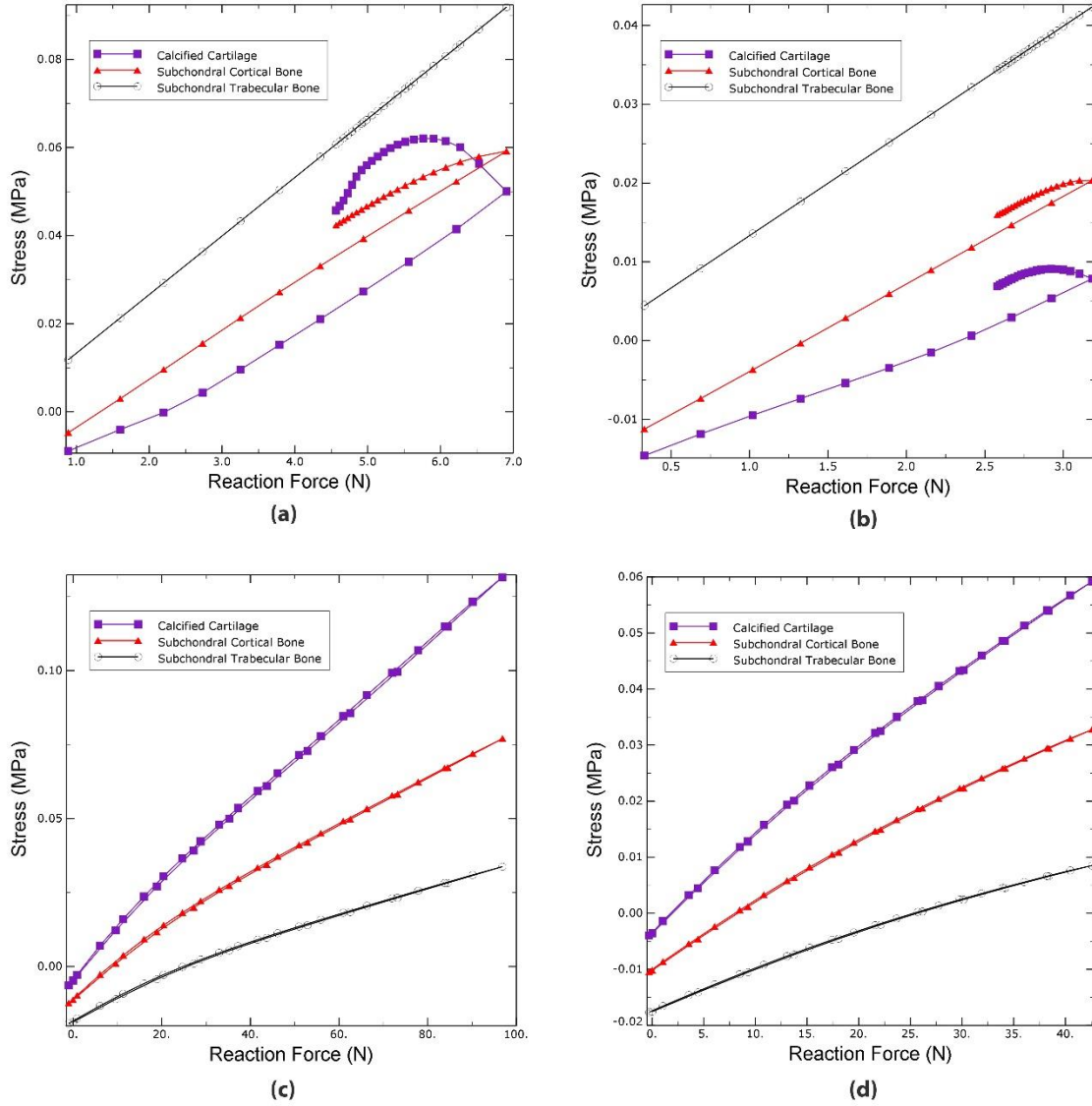Note: The simulation method was aimed at assessing the functionality of BCU multiphasic model, and the result would be different in advanced OA or different loading conditions.

Validation tests

During the UC test, the model could predict the response in the range of the maximum strain of this study (around 10%). Further deformation of the tissue, led to an approximately maximum error of 15% (Figure 9).

The confined compression results represent similar trends in the stress-strain behavior of the tissue constituents, while a roughly fixed difference in the osmotic pressure is observable (around 20 KPa), which originates from the difference in the GAG

formulations. The total stress results, however, are similar to the previous numerical and experimental data (Figure. 10).
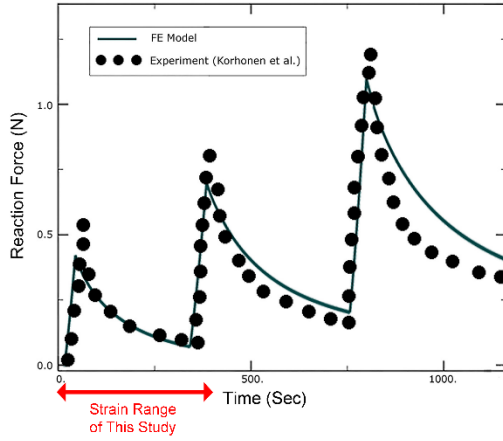

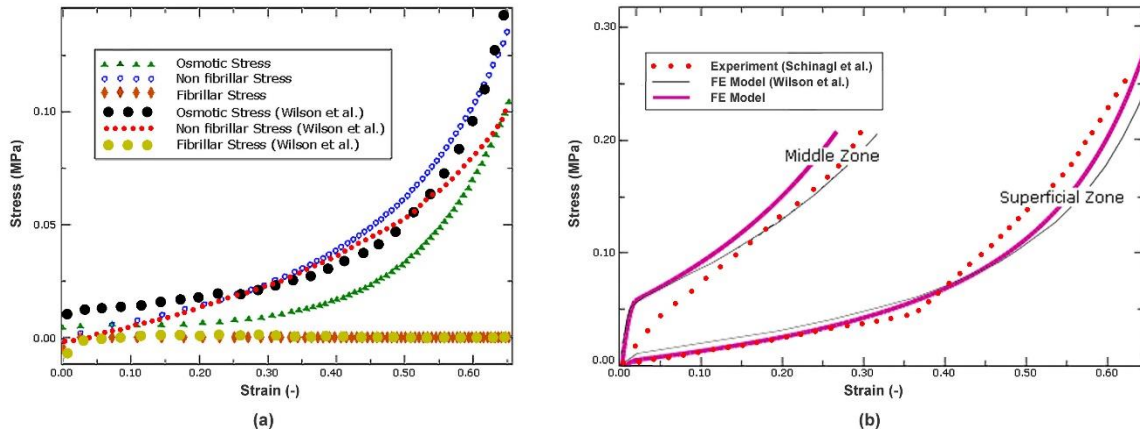Figure 9. Plot of reaction force vs. time in validation UC experiment conducted by Korhonen et al. [56]

Figure 10. Plots of stress-strain behavior, measured from validation simulation of confined compression, proposed by Schinagl et al. [57] and replicated by Wilson et al. [28], in terms of (a) constituent stresses in the AC upper layer and (b) effective stresses.

Discussion

This study proposed a BCU FE model by incorporating some of the validated models [12,28,33] to conduct a multiphasic simulation of the non-advanced OA during a set of UC and indentation tests. The degeneration was studied by altering the dominant changing parameters, which comprised of the collagen softening, permeability and fluid fraction increase. The principal alterations during OA degeneration typically include simultaneous proteoglycan and collagen depletion [11]. Proteoglycans depletion increases the BCU permeability and AC fluid fraction, as well as altering osmotic pressure and solid matrix stiffness [53]. The latter case could be neglected, considering that the non-fibrillar constituent bears inappreciable importance in our simulations [18] (Figure 5). The

13

proteoglycan depletion is discernable only in the SZ during early OA [11]. However, this zone involves lesser osmotic pressure [18] (Figure 6). Therefore, the osmotic material parameters assumed constant during the simulations.

In both of the tests, the OA degeneration reduced the AC osmotic pressure, while its load sharing contributions were dramatically increased, despite the overall osmotic pressure reduction (Figure 7). The fibrillar stress contributions increased, which is interesting as this part was softened, implying that the degeneration transferred more loads from the fluid phase to the fibrillar phase. As the tests were carried out by the displacement control less than 10% strain, the BCU stresses witnessed an unsurprising reduction in stress. Also, CC involves the highest stress variations, implying that CC might be the most important part of subchondral tissues which is in agreement with the previous experimental observations [7,11] (Figure 8).

In the Indentation simulation, the reaction force decreased after OA (Figure 4), which is in contrast to the previous FE simulation [12], as they only considered the permeability increase. Therefore, the recording reaction force was governed by the solid matrix softening in lieu of the 'short circuit' effect, which could surprisingly increase the elasticity in some particular situations [12]. The similar reduction in the reaction forces was also reported in the previous experimental AC study [58]. Additionally, in agreement with some experimental observations [7,59], this simulation put the emphasis on the importance of the mass transport in SBs, considering that the degeneration can severely reduce the fluid permeation through SBs (Figure 3). The result would have been totally different if our model only had encompassed the permeability increase [12]. These conflicting results show the importance of a totally multiphasic simulation.

The accuracy of the proposed FE model was evaluated by comparison of the data from previous works as well as implementing separate studies with this model. First and foremost, the previous validated FE study [18] determined the relative contributions of the healthy AC parts to load bearings under similar compression tests, in which the results for the AC DZ zones indicate that the fluid pressure contributed the most (73% in indentation and 63% in UC), and the remaining loads were mostly supported by the osmotic pressure. These findings are very analogous to the results of the present BCU model (Figure 5), although their fluid pressure parameters took more loads (around a maximum of 20%). Such a difference could be explained by the higher strain rates of the previous study which can turn some of the osmotic pressure to fluid pressure [18]. Secondly, replication of two other experimental tests, including a UC [56] (Figure 9) and confined compression tests [57] (Figure 10), verified the general model fidelity. Finally, the mesh refinement studies were conducted in the indentation simulation, because of the mesh distortions near the boundary, which verified the computational accuracy (Figure 4).

Although this study improved on the general BCU model, it still has some limitations. Firstly, the loading conditions were deliberately chosen in compliance with the previous similar study [60] for the sake of comparison, which did not include all the physiological loads, such as the rotational or shear load types. Moreover, the SB model incorporated a general material description of SBs and the changes in permeability during

OA, which give a better qualitative picture of the OA process in this region in comparison to previous models. Nonetheless, such a general model of SBs is another limitation of this study, as it did not encompass the location-dependent alterations in the geometry and biomaterial parameters of SBs [9], which can quantitatively affect the recorded parameters in subchondral parts [9]. The future studies should be directed toward the simulations with more load conditions along with further details of the material behavior of the tissue [61–65].

In conclusion, the proposed FE model provides some different results in comparison to its simpler counterparts, showing the importance of the multiphasic simulation of BCU OA. In particular, the simulation might reinforce the notion that different SBs play a role in the pathogenesis of OA by reducing the overall fluid permeation. Also, it is shown that the BCU dominant parameters highly influence the OA degeneration, and the relative contribution of the fibrillar part might surprisingly increase by collagen softening. These new results demonstrate the functionality of the proposed general BCU model.

Appendix

In this appendix, the details of the consistent Jacobian tensor derivation for the fibrillar and non-fibrillar AC matrix constituents are presented via a similar approach of the GAG constituent derivation [24,47]. Recalling (11) and using (2), the 2nd Piola–Kirchhoff stress tensor of the fibrillar constituent was simply derived as

$$S_{ij}^{COL} = \phi_0^S \sum_{I=1}^{9} \rho_C^I \left(\frac{E_0 + E_\varepsilon \varepsilon_F^I}{\lambda^I} \varepsilon_F^I N_i^I N_j^I \right) \tag{16}$$

Where N_i^I is the initial fibril direction in the *Ith* fibril that is related to the right Cauchy-Green deformation tensor by

$$N_i^I C_{ij} N_j^I = \left(\lambda^I \right)^2 \tag{17}$$

Recalling (10) and using (16), the fibrillar material elasticity tensor derived as

$${}^4\tilde{C}_{ijkr}^{COL} = \phi_0^S \sum_{I=1}^{9} \left(\frac{\rho_C^I}{\lambda^I} \left[\left(E_0 + 2E_\varepsilon \varepsilon_F^I \right) \left(\frac{\partial \varepsilon_F^I}{\partial C_{kr}} + \frac{\partial \varepsilon_F^I}{\partial C_{rk}} \right) - \frac{E_0 + E_\varepsilon \varepsilon_F^I}{\lambda^I} \left(\frac{\partial \lambda^I}{\partial C_{kr}} + \frac{\partial \lambda^I}{\partial C_{rk}} \right) \varepsilon_F^I \right] N_i^I N_j^I \right) \tag{18}$$

Also, differentiation of the fibrillar logarithmic strain with respect to the right Cauchy-Green deformation tensor yields

$$\frac{\partial \varepsilon_F^I}{\partial \mathbf{C}} = \frac{1}{\lambda^I} \frac{\partial \lambda^I}{\partial \mathbf{C}} \tag{19}$$

And differentiation of equation (17) with respect to elongation yields

$$\frac{\partial \lambda^I}{\partial \mathbf{C}} = \frac{1}{2\lambda^I} N_i^I N_j^I \tag{20}$$

Substituting (19) and (20) into (18) and recalling (9), the fibrillar matrix spatial elasticity tensor yields (14).

On the other hand, the non-fibrillar matrix material elasticity tensor was derived by a similar approach as

$$ {}^4 \tilde{\mathbf{C}}^{MAT} = -2G_M \left(1 - \rho_C^{TOT}\right) \phi_0^S \left(\mathbf{C}^{-1} \frac{\partial \left(J^{2/3} + \frac{\ln J}{6} \left[\frac{3\phi_0^S}{J - \phi_0^S} \left(\frac{J \ln J}{J - \phi_0^S} - 2 \right) - 4 \right] \right)}{\partial \mathbf{C}} + \left(J^{2/3} + \frac{\ln J}{6} \left[\frac{3\phi_0^S}{J - \phi_0^S} \left(\frac{J \ln J}{J - \phi_0^S} - 2 \right) - 4 \right] \right) \frac{\partial \mathbf{C}^{-1}}{\partial \mathbf{C}} \right) \tag{21} $$

This equation requires the following differentiation [66]

$$ \frac{\partial C_{ij}^{-1}}{\partial C_{kr}} = -\frac{1}{2} \left(C_{ik}^{-1} C_{jr}^{-1} + C_{ir}^{-1} C_{jk}^{-1} \right) \tag{22} $$

$$ \frac{\partial (J)}{\partial \mathbf{C}} = \frac{J}{2} \mathbf{C}^{-T} \tag{23} $$

Substituting (22) and (23) into (21) and recalling (9), the non-fibrillar matrix spatial elasticity tensor yields (15).

Acknowledgements

Declaration of conflicting interests

The authors declare no conflict of interest.

Funding

References

1.   Chen A, Gupte C, Akhtar K, et al. The Global Economic Cost of Osteoarthritis: How the UK Compares. *Arthritis* 2012; 2012: 1–6.

2.   Helmick CG, Felson DT, Lawrence RC, et al. Estimates of the prevalence of arthritis and other rheumatic conditions in the United States. Part I. *Arthritis Rheum* 2008; 58: 15–25.

3.   Brandt KD, Radin EL, Dieppe PA, et al. Yet more evidence that osteoarthritis is not a cartilage disease. *Annals of the Rheumatic Diseases*, 2006, pp. 1261–1264.

4.   Felson DT, Neogi T. Osteoarthritis: Is It a Disease of Cartilage or of Bone? *Arthritis and Rheumatism*, 2004, pp. 341–344.

5.   Lories RJ, Luyten FP. The bone–cartilage unit in osteoarthritis. *Nat Rev Rheumatol* 2011; 7: 43–49.

6.   Burr DB. Anatomy and physiology of the mineralized tissues: Role in the pathogenesis of osteoarthrosis. *Osteoarthr Cartil* 2004; 12: 20–30.

7.   Hwang J, Bae WC, Shieu W, et al. Increased hydraulic conductance of human articular cartilage and subchondral bone plate with progression of osteoarthritis. *Arthritis Rheum* 2008; 58: 3831–42.

8.   Paietta RC, Burger EL, Ferguson VL. Mineralization and collagen orientation throughout aging at the vertebral endplate in the human lumbar spine. *J Struct Biol* 2013; 184: 310–320.

9.   Venäläinen MS, Mononen ME, Jurvelin JS, et al. Importance of Material Properties and Porosity of Bone on Mechanical Response of Articular Cartilage in Human Knee Joint—A Two-Dimensional Finite Element Study. *J Biomech Eng* 2014; 136: 121005.

10.   Madry H, van Dijk CN, Mueller-Gerbl M. The basic science of the subchondral bone. *Knee Surgery, Sport Traumatol Arthrosc* 2010; 18: 419–433.

11.   Saarakkala S, Julkunen P, Kiviranta P, et al. Depth-wise progression of osteoarthritis in human articular cartilage: investigation of composition, structure and biomechanics. *Osteoarthr Cartil* 2010; 18: 73–81.

12.   Stender ME, Regueiro RA, Ferguson VL. A poroelastic finite element model of the bone–cartilage unit to determine the effects of changes in permeability with osteoarthritis. *Comput Methods Biomech Biomed Engin* 2016; 1–13.

13.   Stender ME, Carpenter RD, Regueiro RA, et al. An evolutionary model of

osteoarthritis including articular cartilage damage, and bone remodeling in a computational study. *J Biomech* 2016; 49: 3502–3508.

14. Jurvelin JS, Buschmann MD, Hunziker EB. Mechanical anisotropy of the human knee articular cartilage in compression. *Proc Inst Mech Eng Part H J Eng Med* 2003; 217: 215–219.

15. Hosseini SM, Wu Y, Ito K, et al. The importance of superficial collagen fibrils for the function of articular cartilage. *Biomech Model Mechanobiol* 2014; 13: 41–51.

16. Korhonen RK, Jurvelin JS. Compressive and tensile properties of articular cartilage in axial loading are modulated differently by osmotic environment. *Med Eng Phys* 2010; 32: 155–160.

17. Katta J, Stapleton T, Ingham E, et al. The effect of glycosaminoglycan depletion on the friction and deformation of articular cartilage. *Proc Inst Mech Eng Part H J Eng Med* 2008; 222: 1–11.

18. Quiroga JMPP, Wilson W, Ito K, et al. Relative contribution of articular cartilage's constitutive components to load support depending on strain rate. *Biomech Model Mechanobiol* 2017; 16: 151–158.

19. Sakai N, Hashimoto C, Yarimitsu S, et al. A functional effect of the superficial mechanical properties of articular cartilage as a load bearing system in a sliding condition. *Biosurface and Biotribology* 2016; 2: 26–39.

20. Lai WM, Mow VC. Drag-induced compression of articular cartilage during a permeation experiment. *Biorheology* 1980; 17: 111–123.

21. Freutel M, Schmidt H, Dürselen L, et al. Finite element modeling of soft tissues: Material models, tissue interaction and challenges. *Clin Biomech* 2014; 29: 363–372.

22. Bae JY, Park KS, Seon JK, et al. Biomechanical analysis of the effects of medial

meniscectomy on degenerative osteoarthritis. *Med Biol Eng Comput* 2012; 50: 53–60.

23.   Jones B, Hung CT, Ateshian G. Biphasic Analysis of Cartilage Stresses in the Patellofemoral Joint. *J Knee Surg* 2015; 29: 92–98.

24.   Stender ME, Raub CB, Yamauchi KA, et al. Integrating qPLM and biomechanical test data with an anisotropic fiber distribution model and predictions of TGF-β1 and IGF-1 regulation of articular cartilage fiber modulus. *Biomech Model Mechanobiol* 2012; 12: 1073–1088.

25.   Mow VC, Guo XE. Mechano-Electrochemical Properties Of Articular Cartilage: Their Inhomogeneities and Anisotropies. *Annu Rev Biomed Eng* 2002; 4: 175–209.

26.   Párraga Quiroga JM, Wilson W, Ito K, et al. The effect of loading rate on the development of early damage in articular cartilage. *Biomech Model Mechanobiol* 2017; 16: 263–273.

27.   Mow VC, Kuei SC, Lai WM, et al. Biphasic Creep and Stress Relaxation of Articular Cartilage in Compression: Theory and Experiments. *J Biomech Eng* 1980; 102: 73.

28.   Wilson W, Huyghe JM, Van Donkelaar CC. Depth-dependent Compressive Equilibrium Properties of Articular Cartilage Explained by its Composition. *Biomech Model Mechanobiol* 2007; 6: 43–53.

29.   Li LP, Herzog W. The role of viscoelasticity of collagen fibers in articular cartilage: theory and numerical formulation. *Biorheology* 2004; 41: 181–194.

30.   Benninghoff A. Form und Bau der Gelenkknorpel in ihren Beziehungen zur Funktion. *Z Anat Entwicklungsgesch* 1925; 76: 43–63.

31.   Wilson W, van Donkelaar CC, van Rietbergen B, et al. Stresses in the local collagen network of articular cartilage: a poroviscoelastic fibril-reinforced finite

element study. *J Biomech* 2004; 37: 357–66.

32. Wilson W, van Donkelaar CC, van Rietbergen B, et al. A fibril-reinforced poroviscoelastic swelling model for articular cartilage. *J Biomech* 2005; 38: 1195–1204.

33. Oungoulian SR, Chen SS, Davol A, et al. Extended Two Compartmental Swelling Stress Model and Isotropic Cauchy Stress Equation for Articular Cartilage Proteoglycans. In: *ASME 2007 Summer Bioengineering Conference*. 2007, p. 847.

34. Buschmann MD, Grodzinsky AJ. A Molecular Model of Proteoglycan-Associated Electrostatic Forces in Cartilage Mechanics. *J Biomech Eng* 1995; 117: 179.

35. Ateshian GAA, Warden WHH, Kim JJJ, et al. Finite deformation biphasic material properties of bovine articular cartilage from confined compression experiments. *J Biomech* 1997; 30: 1157–1164.

36. Wu JZ, Herzog W. Finite element simulation of location- and time-dependent mechanical behavior of chondrocytes in unconfined compression tests. *Ann Biomed Eng* 2000; 28: 318–30.

37. Holmes MHH, Mow VC. The nonlinear characteristics of soft gels and hydrated connective tissues in ultrafiltration. *J Biomech* 1990; 23: 1145–1156.

38. van der Voet A. A comparison of finite element codes for the solution of biphasic poroelastic problems. *Proc Inst Mech Eng H* 1997; 211: 209–11.

39. Borchers L, Reichart P. Three-dimensional Stress Distribution Around a Dental Implant at Different Stages of Interface Development. *J Dent Res* 1983; 62: 155–159.

40. Morgan EF, Keaveny TM. Dependence of yield strain of human trabecular bone on anatomic site. *J Biomech* 2001; 34: 569–577.

41. Mente PL, Lewis JL. Elastic modulus of calcified cartilage is an order of magnitude less than that of subchondral bone. *J Orthop Res* 1994; 12: 637–647.

42. Brocklehurst R, Bayliss MT, Maroudas A, et al. The composition of normal and osteoarthritic articular cartilage from human knee joints. *J Bone Joint Surg Am* 1984; 66: 95–106.

43. Setton LA, Mow VC, Howell DS. Mechanical behavior of articular cartilage in shear is altered by transection of the anterior cruciate ligament. *J Orthop Res* 1995; 13: 473–482.

44. Wei X, Räsänen T, Messner K. Maturation-related compressive properties of rabbit knee articular cartilage and volume fraction of subchondral tissue. *Osteoarthr Cartil* 1998; 6: 400–409.

45. Nauman EA, Fong KE, Keaveny TM. Dependence of Intertrabecular Permeability on Flow Direction and Anatomic Site. *Ann Biomed Eng* 1999; 27: 517–524.

46. Chen SS, Falcovitz YH, Schneiderman R, et al. Depth-dependent compressive properties of normal aged human femoral head articular cartilage: Relationship to fixed charge density. *Osteoarthr Cartil* 2001; 9: 561–569.

47. Taffetani M, Griebel M, Gastaldi D, et al. Poroviscoelastic finite element model including continuous fiber distribution for the simulation of nanoindentation tests on articular cartilage. *J Mech Behav Biomed Mater* 2014; 32: 17–30.

48. Lipshitz H, Etheredge R, Glimcher MJ. In vitro wear of articular cartilage. *J Bone Joint Surg Am* 1975; 57: 527–34.

49. Rieppo J. Poster: Spatial Determination of Water, Collagen and Proteogycan Content by Fourier Transform Infrared Imaging and Digital Densitometry. *50th Annu Meet Orthop Res Soc* 2004; Poster No: 1021.

50. Shapiro EM, Borthakur A, Kaufman JH, et al. Water distribution patterns inside

bovine articular cartilage as visualized by 1H magnetic resonance imaging. *Osteoarthr Cartil* 2001; 9: 533–538.

51.   Mononen ME, Julkunen P, Töyräs J, et al. Alterations in structure and properties of collagen network of osteoarthritic and repaired cartilage modify knee joint stresses. *Biomech Model Mechanobiol* 2011; 10: 357–369.

52.   Julkunen P, Wilson W, Jurvelin JS, et al. Stress-relaxation of human patellar articular cartilage in unconfined compression: Prediction of mechanical response by tissue composition and structure. *J Biomech* 2008; 41: 1978–1986.

53.   Korhonen RK, Laasanen MS, Töyräs J, et al. Fibril reinforced poroelastic model predicts specifically mechanical behavior of normal, proteoglycan depleted and collagen degraded articular cartilage. *J Biomech* 2003; 36: 1373–1379.

54.   Nguyen N, Waas AM. Nonlinear, finite deformation, finite element analysis. *Zeitschrift für Angew Math und Phys* 2016; 67: 35.

55.   Pawaskar SS, Fisher J, Jin Z. Robust and General Method for Determining Surface Fluid Flow Boundary Conditions in Articular Cartilage Contact Mechanics Modeling. *J Biomech Eng* 2010; 132: 031001.

56.   Korhonen RK, Laasanen MS, Töyräs J, et al. Comparison of the equilibrium response of articular cartilage in unconfined compression, confined compression and indentation. *J Biomech* 2002; 35: 903–909.

57.   Schinagl RM, Gurskis D, Chen AC, et al. Depth-dependent confined compression modulus of full-thickness bovine articular cartilage. *J Orthop Res* 1997; 15: 499–506.

58.   Robinson DL, Kersh ME, Walsh NC, et al. Mechanical properties of normal and osteoarthritic human articular cartilage. *J Mech Behav Biomed Mater* 2016; 61: 96–109.

59.   Pan J, Zhou X, Li W, et al. In situ measurement of transport between subchondral bone and articular cartilage. *J Orthop Res* 2009; 27: 1347–1352.

60.   Connolly A, FitzPatrick D, Moulton J, et al. Tibiofemoral cartilage thickness distribution and its correlation with anthropometric variables. *Proc Inst Mech Eng Part H J Eng Med* 2008; 222: 29–39.

61.   Bell CJ, Ingham E, Fisher J. Influence of hyaluronic acid on the time-dependent friction response of articular cartilage under different conditions. *Proc Inst Mech Eng Part H J Eng Med* 2006; 220: 23–31.

62.   Wang L, Kalu DN, Banu J, et al. Effects of Ageing on the Biomechanical Properties of Rat Articular Cartilage. *Proc Inst Mech Eng Part H J Eng Med* 2006; 220: 573–578.

63.   Mohammadi H, Mequanint K, Herzog W. A p-type finite element solution for the simulation of O_2 transport in articular cartilage tissue: heterogeneous and porous media. *Proc Inst Mech Eng Part H J Eng Med* 2011; 225: 1003–1014.

64.   Sadeghi H, Espino DM, Shepherd DE. Variation in viscoelastic properties of bovine articular cartilage below, up to and above healthy gait-relevant loading frequencies. *Proc Inst Mech Eng Part H J Eng Med* 2015; 229: 115–123.

65.   Pierce DM, Unterberger MJ, Trobin W, et al. A microstructurally based continuum model of cartilage viscoelasticity and permeability incorporating measured statistical fiber orientations. *Biomech Model Mechanobiol* 2016; 15: 229–244.

66.   Bonet J, Wood RD. Nonlinear Continuum Mechanics for Finite Element Analysis. *Commun Numer Methods Eng* 1997; 24: 1567–1568.